

Ultra-compact nonvolatile photonics based on electrically reprogrammable transparent phase change materials

Carlos Ríos^{1,†,*}, Qingsyang Du^{1,†}, Yifei Zhang¹, Cosmin-Constantin Popescu¹, Mikhail Y. Shalaginov¹, Paul Miller², Christopher Roberts², Myungkoo Kang³, Kathleen A. Richardson³, Tian Gu⁴, Steven A. Vitale², Juejun Hu^{1,4,*}

¹*Department of Materials Science & Engineering, Massachusetts Institute of Technology, Cambridge, MA, USA*

²*Lincoln Laboratory, Massachusetts Institute of Technology, Lexington, MA, USA*

³*The College of Optics & Photonics, Department of Materials Science and Engineering, University of Central Florida, Orlando, FL USA*

⁴*Materials Research Laboratory, Massachusetts Institute of Technology, Cambridge, MA, USA*

[†]*These authors contributed equally*

**carios@mit.edu, hujuejun@mit.edu*

Abstract

Energy-efficient programmable photonic integrated circuits (PICs) are the cornerstone of on-chip classical and quantum optical technologies.^{1,2} Optical phase shifters constitute the fundamental building blocks which enable these programmable PICs. Thus far, carrier modulation and thermo-optical effect are the chosen phenomena for ultrafast and low-loss phase shifters, respectively; however, the state and information they carry are lost once the power is turned off—they are volatile. The volatility not only compromises energy efficiency due to their demand for constant power supply, but also precludes them from emerging applications such as in-memory computing. To circumvent this limitation, we introduce a novel phase shifting mechanism that exploits the nonvolatile refractive index modulation upon structural phase transition of Sb₂Se₃, an ultralow-loss phase change material. A zero-static power and electrically-driven phase shifter was realized on a foundry-processed silicon-on-insulator platform, featuring record phase modulation up to 0.09 π/μm and a low insertion loss of 0.3 dB/π. We further pioneered a one-step partial amorphization scheme to enhance speed and energy efficiency of PCM devices. A diverse cohort of programmable photonic devices were demonstrated based on the ultracompact PCM phase shifter.

The ability to actively control the phase of light is the common denominator in applications ranging from optical switching in data communications^{3,4}, beam steering,⁵ spectroscopy,⁶ optical neural networks,⁷ and quantum processing and computing with single photons.⁸ Phase modulation has been achieved with carrier injection or depletion in semiconductors;^{9,10}, electrooptic (EO) effects in liquid crystals,^{11,12} EO polymers,¹³ and Pockels crystals¹⁴; thermo-optic (TO) effect;^{15,16} and mechanical displacement.¹⁷ The small refractive index perturbation from these mechanisms results in a large device footprint, often hundreds of microns or larger (Table 1). Other limitations include significant optical loss penalty (carrier injection/depletion), long switching time (liquid crystals), as well as challenges associated with standard foundry process integration (EO polymers, Pockels crystals, and mechanical displacement). Moreover, all

the mechanisms above are volatile, mandating constant power supply to operate. Such volatility significantly increases energy consumption, especially for applications where reconfiguration operations occur only at millisecond intervals or even longer. Nonvolatile phase shifters for PICs have been achieved with charge-trapping effects,¹⁸ mechanically latched micro-electromechanical systems,¹⁹ and ferroelectric domain switching,²⁰ which thus far have suffered from high-losses, severe long-term drift, large form factors, or CMOS incompatibility. A compact, low-loss, and nonvolatile optical phase shifter (OPS) compatible with CMOS chip integration is therefore much coveted.

Chalcogenide phase change materials (PCMs) offer a promising solution to nonvolatile programmable PICs.^{21–23} Traditional PCM devices, however, cannot offer phase-only modulation due to high optical losses associated with classical PCMs exemplified by Ge₂Sb₂Te₅.²⁴ Moreover, most PCM device prototypes to date still rely upon furnace annealing or external laser excitation to trigger the structural transition. The limitation has motivated the development of low-loss PCMs in recent years such as Ge₂Sb₂Se₄Te (GSST),²⁵ Sb₂S₃,²⁶ and Sb₂Se₃.²⁷ In particular, Sb₂Se₃ offers vanishingly small losses at 1550 nm and an index contrast $\Delta n \approx 0.77$,²⁷ making it an ideal PCM for programmable photonics in the telecommunication bands. Capitalizing on the unique attributes of Sb₂Se₃, this work demonstrates an OPS that simultaneously confers low insertion loss, small form factor, and zero-static power consumption. The OPS devices were fabricated in silicon-on-insulator (SOI) where silicon acts both as the light guide and resistive heater to actuate structural phase transition via single electrical pulses. Importantly, the devices were processed on 200-mm wafers leveraging a 90-nm CMOS foundry, enabling them to be seamlessly integrated with industry-standard PIC platforms.

Results

The PCM-based phase shifter comprises a 30 nm Sb₂Se₃ cell, initially prepared in the crystalline state, resting on top of a half-etched SOI ridge waveguide. A section of the waveguide was phosphorus-doped to act as a microheater (Fig. 1a). More details of the foundry fabrication process are described in Methods. An essential aspect of the microheater design is the choice of doping concentration given the trade-off between resistivity and optical losses (Fig. 1b). Lower resistivity reduces the pulse voltages required to reach the transition temperatures of Sb₂Se₃ at the expense of exacerbated free carrier absorption. After testing four different doping combinations, we found a good balance with a concentration of $n \sim 4 \times 10^{18} \text{ cm}^{-3}$, which corresponds to an insertion loss of $\sim 0.01 \text{ dB}/\mu\text{m}$. Fig. 1c shows a scanning electron microscope image of a phase shifter with a 10 μm -long bowtie-shaped doping region. With a refractive index contrast $\Delta n \approx 0.77$ upon switching (Fig. 1d), a mode simulation indicates a change in effective refractive index equaling to $\Delta n_{\text{eff}} \approx 0.071$ and a phase shift of $0.09 \pi/\mu\text{m}$. This corresponds to an ultra-compact OPS of only 11 μm in length needed to attain full π phase delay, representing significant improvement over the state-of-the-art. The small device footprint also yields a low theoretical insertion loss of 0.1 dB resulting from free carrier

absorption. Experimentally, we measured a total insertion loss of 0.03 dB/ μm , with a negligible 0.0005 dB/ μm change upon Sb_2Se_3 phase transition. The loss is more significant than the expected value due to other effects such as scattering.

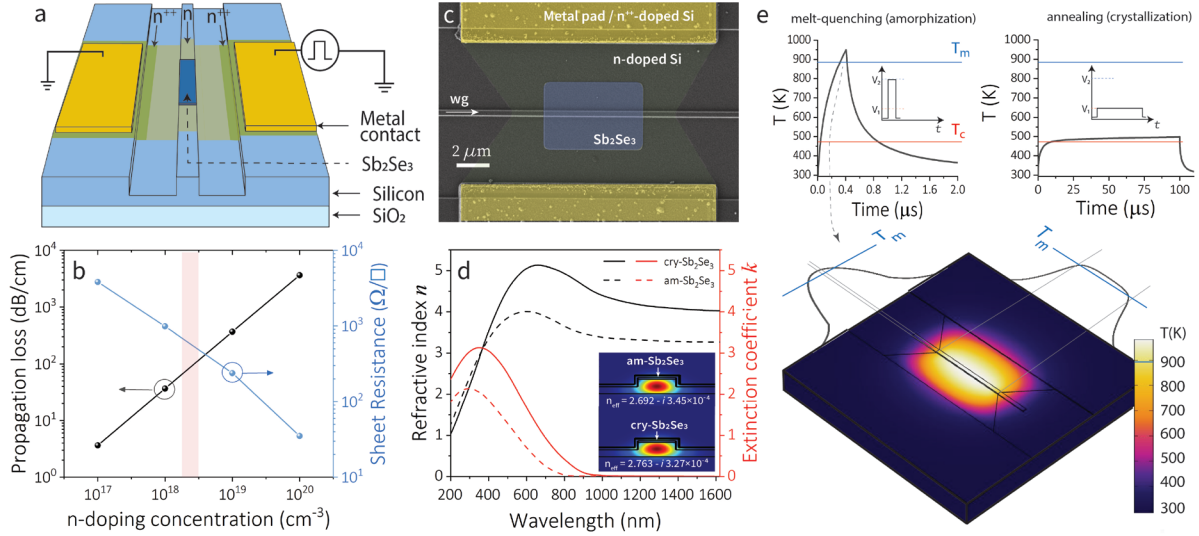


Fig. 1. Sb₂Se₃-based phase shifter using a doped-silicon microheater: **a** microheater design with doped-silicon profiles to create an electrical resistor in a half-etched 220nm SOI waveguide. **b** FEM simulated propagation loss and sheet resistivity as a function of phosphorous doping concentration. The highlighted region corresponds to the doping concentration used in this work. **c** Colored SEM image of a fabricated 10 μm -long bowtie microheater with a 6 μm -long Sb₂Se₃. **d** Sb₂Se₃ refractive index in both amorphous and crystalline states with simulated optical modes for each state at 1565 nm wavelength. **e**. FEM simulated transient temperature during and after the pulse excitation for both amorphization and crystallization. The 3D plot shows the temperature profile at the end of the amorphization pulse, reaching the melting temperature of Sb₂Se₃.

To reversibly switch, we use Joule heating induced by a voltage pulse that elevates the temperature of the central area of the microheater, which coincides with the waveguide. The pulse width and voltage depend on the geometry of the microheater. For the bowtie geometry in Fig. 1c, which we will extensively use throughout this work for $\pi/2$ phase shift, we used 3.2 V (3 mA) pulses of varying widths (up to 1 ms) to crystallize either partially or entirely by heating to above the crystallization temperature, $T_c = 200$ °C. To amorphize, a single 21 V (7.8 mA) \times 400 ns pulse was employed to raise the temperature over the melting point, $T_m = 620$ °C. The large voltage required to amorphize results from the non-ohmic behavior of the resistance for large voltages, given the strong dependence of the carrier mobility on temperature. Fig. 1e shows a COMSOL Multiphysics simulation of the temperature evolution for both the amorphization and crystallization pulses and the 3D temperature profile at the end of the amorphization pulse. According to the simulations, our design allows reversible switching of Sb₂Se₃ along the waveguide in almost its entire length – 9 μm out of 10 μm -long microheater where $T > T_m$. Given the large thermal conductivity of silicon, heat is rapidly dissipated after the pulse excitation with a decay time of 400 ns, allowing the fast quench process required to amorphize Sb₂Se₃. We found that the most prolonged pulse duration able to amorphize was around 1 μs , beyond which crystallization cannot be suppressed entirely during cooling.

We initially demonstrate phase modulation using an unbalanced MZI with a 10 μm -long Sb_2Se_3 OPS in each arm. Each phase shifter introduces $\sim 0.8\pi$ phase shift leading to a total dynamic phase modulation in the $[-0.8\pi, 0.8\pi]$ range. Fig. 2b shows the four permutations for the extreme phase states; however, we also achieve continuous (multi-state) switching by partially crystallizing amorphous Sb_2Se_3 . We further demonstrate a 2×2 switch – a basic building block for constructing programmable photonic architectures¹ – in which light can be switched between two outputs by applying $\pm \pi/2$ phase shift in both arms. Using an ultra-compact 10 μm -long heater with 6 μm -long Sb_2Se_3 , we show up to 250 switching events (125 complete cycles) from the transmission difference between each output arm (Fig. 2c). Reversible and reliable switching of each phase shifter allows achieving the four different ‘full’ phase permutations, including splitting equally or directing the light to each of the two output channels with up to 15 dB extinction ratio (Fig. 2d). An unbalanced directional coupler causes the difference in extinction ratio (ER) between the two opposite phase states at the output of the MZI, but the $\pi/2$ phase shift is verified in each arm.

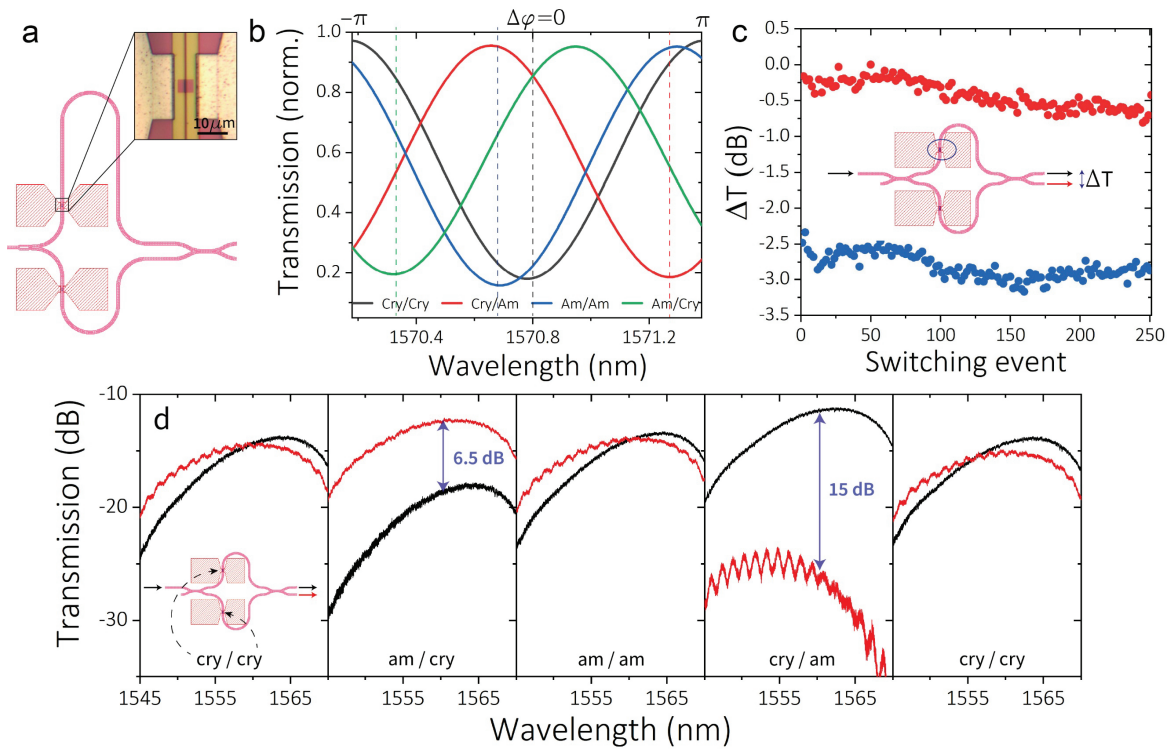


Fig. 2. Sb_2Se_3 -based phase shifters in balanced (2×2 switch) and unbalanced MZI devices. **a** layout of an unbalanced MZI with an optical microscope image of a 6 μm Sb_2Se_3 cell. **b** Experimental demonstration of the four interferograms corresponding to each phase state permutation of two 10 μm -long Sb_2Se_3 OPS in the device shown in **a**. Full crystallization was achieved using 3.2 V and 1 ms pulses. Amorphization was achieved with 21 V and 400 ns pulses. **c** Reversible switching over 125 full cycles between two intermediate Sb_2Se_3 states of the top-arm phase shifter in a balanced MZI. The plotted changes in transmission correspond to the difference between each arm’s intensity. **d** MZI 2×2 switch in the four different permutations: amorphous and crystalline states of each arm’s phase shifter with 6 μm Sb_2Se_3 cell for $\pi/2$ shift. Reversible switching is demonstrated for both cells. Black and red represents the top and bottom output ports, respectively (see inset).

We now introduce Sb_2Se_3 -based phase shifters in micro-ring resonators (Fig. 3a). Like MZI devices, we demonstrate continuous, multi-state modulation of an all-pass resonator by partially crystallizing a 3 μm -long Sb_2Se_3 cell (Fig. 3b). Fig. 3c shows the reversible switching of the cell in 10 cycles between fully amorphous and fully crystalline states with remarkable reproducibility and excellent agreement with the theoretical $0.09 \pi/\mu\text{m}$ value. The losses upon crystallization were 5 dB/cm, which is negligible compared to the free carrier absorption but enough to vary the extinction ratio of the resonance peaks slightly by modulating the coupling amplitude. We then measured micro-ring resonators with an add-drop configuration and a 6 μm -long Sb_2Se_3 cell (Fig. 3d). Fig. 3e and 3f demonstrate the phase-only modulation changing the resonance wavelength of the through-port dip or drop-port peak and the $\sim \pi/2$ phase modulation of the ultra-compact device. This type of device can be used as wavelength filters with precise tunability and nonvolatile response.

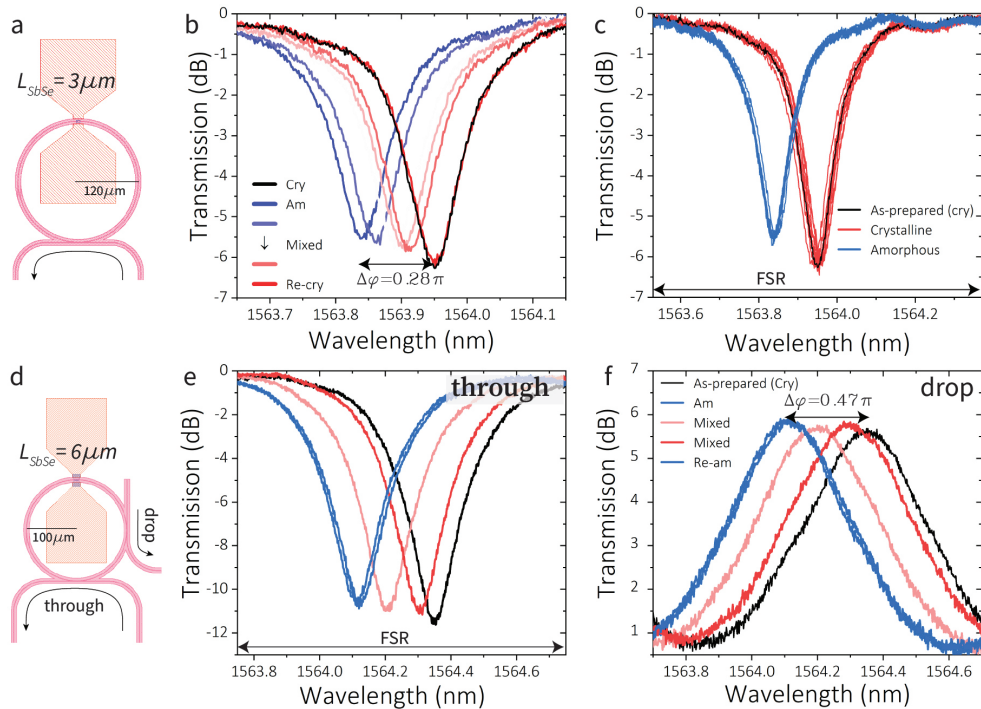


Figure 3. Reversible and multi-level switching of Sb_2Se_3 phase shifters in micro-ring resonators. **a** layout of a 120 μm -radius, 200 nm-gap micro-ring resonator with a 6 μm -long Sb_2Se_3 cell. This device is used to experimentally demonstrate **b** one full reversible cycle featuring some of the partial crystallization states and a total of 0.28π shift, in excellent agreement with the expected $0.09 \pi/\mu\text{m}$, and **c** ten full cycles with excellent reproducibility. **d** Same ring resonator as in **a** featuring a drop port identical to the main coupling port. **e** Demonstration of phase shift of resonance dip modulation in the through port with up to 10 dB in ER modulation. **f** Drop port peaks for the same exact measurements shown in **e** with a total phase shift of 0.47π . 3.2 V and 100 μs - 1ms pulses were used to partially crystallize and a single 21 V and 400 ns pulse was used to fully amorphize.

In addition to spectral detuning of the resonant peak, we also demonstrate that the phase shifter can be applied to extinction ratio modulation by tuning the waveguide effective index at the coupling region, which modifies the coupling coefficient between the ring and the waveguide (Fig. 4a)²⁸. We explored the two different configurations shown in Fig. 4b and 4c with Sb_2Se_3 cells covering either the ring waveguide only or both waveguides, respectively. The latter was more effective at introducing significant variations in both extinction ratio ($\sim 20\text{dB}$ change, closer to critical coupling) and resonance wavelength (close to the expected $\pi/2$ phase shift); whereas the former showed an amplitude modulation with a damped phase modulation in the through port. Simultaneous amplitude and phase trimming, as we will show later in this paper, are potential applications of Sb_2Se_3 -based phase shifters, allowing correct fabrication variations in the targeted resonance wavelength and the intended coupling regime.

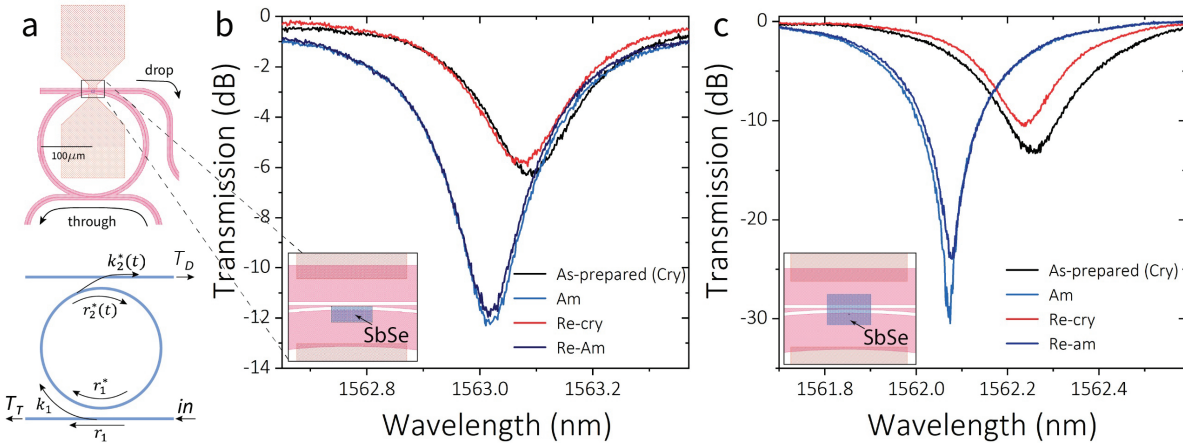


Figure 4. Extinction ratio tuning via phase-shift triggered coupling coefficient modulation. **a** Schematic of the ring resonators under test with a drop port at the phase shifter position and the corresponding modulation of the coupling coefficients k and r . **b** Experimental results for the device through port for two switching cycles of a Sb_2Se_3 cell placed on the ring waveguide only, as shown in the inset. **c** Same as **b** for a Sb_2Se_3 cell covering both the ring waveguide and the drop port with nearly 20 dB modulation in ER.

Up to this point, we have shown Sb_2Se_3 phase shifters capable of performing partial recrystallization to achieve intermediate states by modulating the number and the width of the crystallization pulses. As a result, when reconfiguring the OPS to a state with lower crystallinity, at least two pulses are needed, where one fully amorphizes and ‘reset’ the material and the other partially crystallizes the PCM. This not only complicates the switching scheme but also significantly compromises the switching speed and energy efficiency, given that crystallization pulses are inherently much longer than the amorphization pulse.²⁹ A switching approach that enables such fast bidirectional tunability is therefore strongly preferred. Here we demonstrate a unique single-step partial amorphization scheme by engineering the temperature profile across a microheater. For this purpose, a microheater shown in Fig. 5a and 5b consisting of five n -doped ‘bridges’ of 2 μm in width, 10 μm in length (connecting both n^{++} regions) was employed. Sb_2Se_3 is only deposited directly on top of each bridge. By changing the pulse width, the temperature profile along the waveguide and across the ‘bridges’ leads to melting temperatures initially

only in the central ‘bridge,’ but then expanding to the outer ones as the pulse width (i.e., energy dissipation) increases. This response, in turn, allows for partial amorphization of the Sb_2Se_3 cells, and with this, different optical responses and phase shifting – analog to the partial amorphization carried out with optical pulses in absorptive PCMs.³⁰ With a total resistance of $1025 \pm 25 \Omega$, the pulse width to start inducing amorphization was $800 \mu\text{s}$ with 21 V . By varying the pulse width, W , from 800 to $1050 \mu\text{s}$; we demonstrate partial amorphization of Sb_2Se_3 in an unbalanced MZI (Fig. 5c) and a micro-ring resonator (Fig. 5d). In Fig. 5c, we show reversible switching between an intermediate state achieved with a $900 \mu\text{s}$ pulse and the fully crystalline state. In our geometry, however, we were only able to reversible switch the three central Sb_2Se_3 cells achieving phase shifts up to $\pi/2$ instead of the 0.9π corresponding to the total $10 \mu\text{m}$ Sb_2Se_3 . Experimentally, we found that ablation occurs before full amorphization is achieved in the outer ‘bridges,’ which is expected from the simulated temperature profiles in Fig. 5a. However, the same concept of leveraging temperature gradient to achieve precisely controlled partial amorphization can be readily extended to other heater designs with more tuning levels and full reversibility.

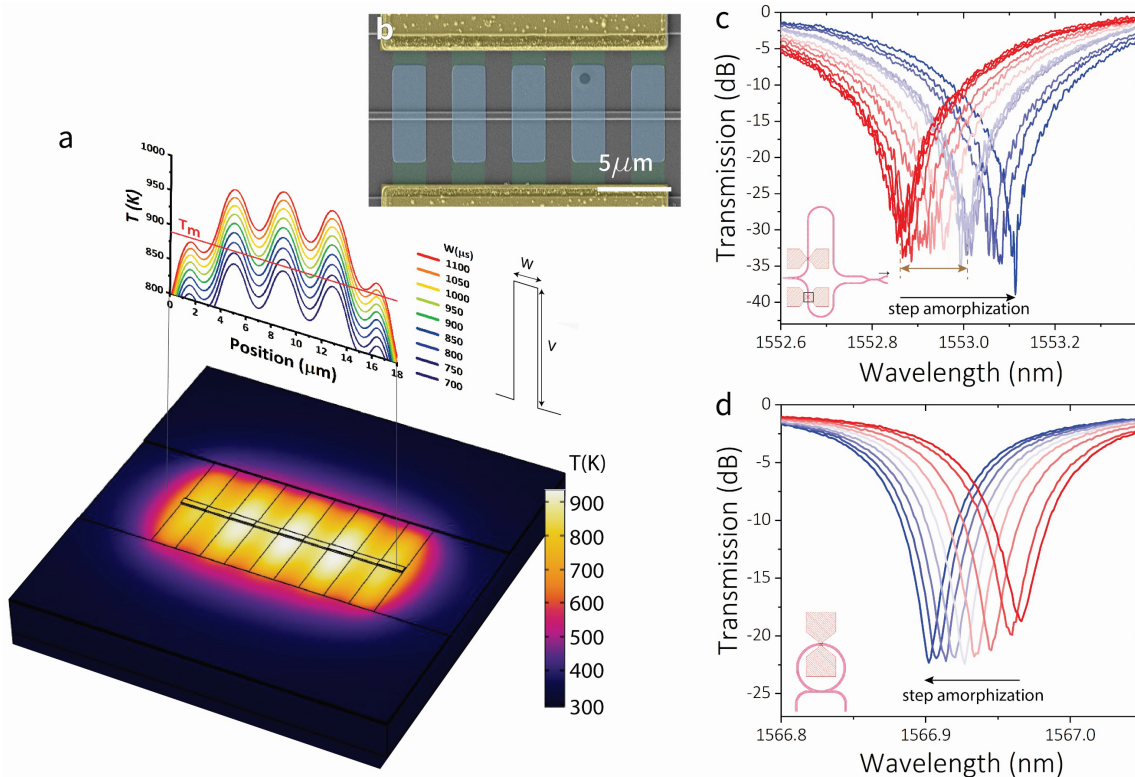


Figure 5. Engineering microheater to achieve partial amorphization. **a** FEM heat transfer simulation of a microheater consisting of five $2 \mu\text{m}$ -wide ‘bridges’. The temperature profile along the waveguide is plotted for different pulse widths. **b** Colored SEM image of a fabricated device. **c** Partial amorphization of the bottom arm Sb_2Se_3 in an unbalanced MZI. 21 V pulses with varying widths between $800 \mu\text{s}$ and $1050 \mu\text{s}$ were employed to amorphize and 3.2 V for 1 ms to fully crystallize. The transmission is measured in the top output waveguide where a maximum of $\pi/2$ phase shift is observed, corresponding to the full amorphization of the three central ‘bridges’. Reversible switching is demonstrated over three cycles between the full crystalline state and the marked intermediate state (corresponding to a $900 \mu\text{s}$ pulse). **d** Same phase shifter with partial amorphization in a micro-ring resonator with continuous tuning of the resonance wavelength.

Bidirectional tuning by partial amorphization and partial crystallization is then possible using phase shifters with a bridge-like structure. Using these microheaters and the pulse sequences previously described, we lastly demonstrate an application that exploits the nonvolatile nature of chalcogenide PCMs: optical device trimming. We use a device comprising two micro-ring resonators connected to a single bus waveguide (Fig. 6) to show the potential of PCMs in countering the optical response variations resulting from chip and wafer non-uniformities. By tuning the phase of one of the micro-ring resonators and keeping the second as a reference, we demonstrate that a nonvolatile phase shift can be used to either isolate each ring's response (Fig. 6a) or to make them coincide by precisely tuning the resonance wavelength until matching (Fig. 6b). Furthermore, Fig. 6c shows how both amorphization and crystallization processes can be combined to shift the peak position in both directions and correct any undesired over-shift if the goal is for the peaks to match. Once the trimming is completed, and thanks to the well-known drift-free optical properties of PCMs,^{21,31} the final optical response is held stable over time, as we demonstrate up to 4×10^6 s (i.e., 47 days) with a slight 0.01nm shift due to temperature fluctuations. More importantly, our low-loss phase shifter still offers the option of recalibrating or changing the configuration later without any power consumption in between.

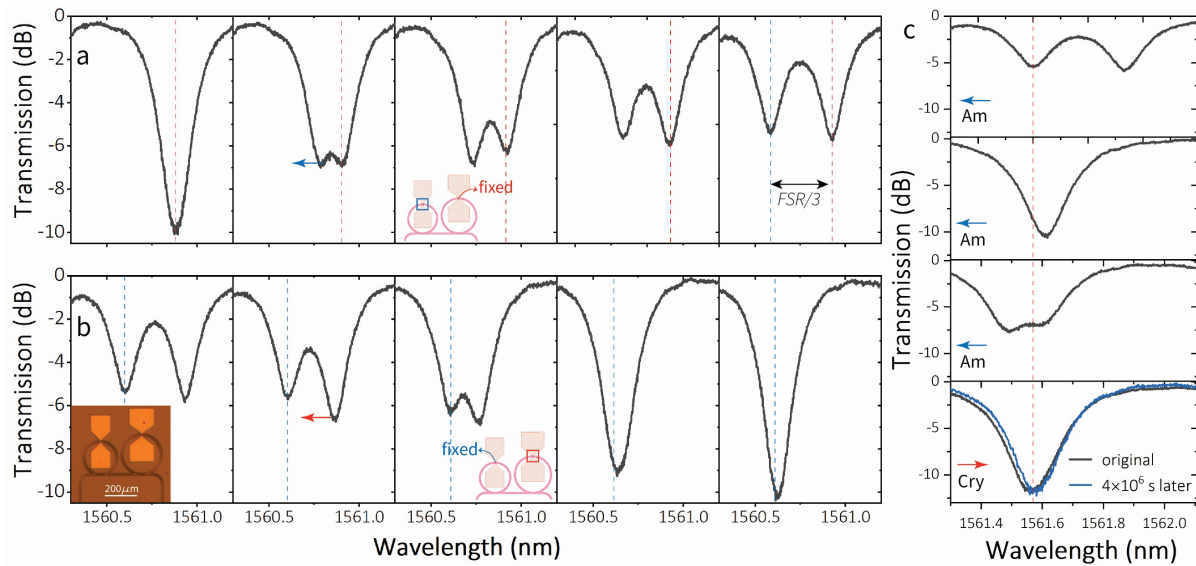


Figure 6. Optical trimming of micro-ring resonators. **a** Detuning of two initially superimposed resonance dips corresponding to two micro-ring resonators with 100 μm (blue line) and 120 μm (red line) in radius connected to a common bus waveguide. The largest ring is left fixed while the smaller ring is phase-shifted via step amorphization to fully isolate the response of each ring. **b** Trimming of the 120 μm micro-ring to match the resonance dip of the smaller ring (fixed), thus, correcting the detuning in **a** but with an overall wavelength shift of 0.6nm. The inset shows an optical microscope image of the actual device. **c** Demonstration of combined amorphization and crystallization to properly trim one micro-ring resonator and compensate 'over-shifting'. Nonvolatile, drift-free response is demonstrated in the last state of the device (bottom panel) by comparing the original and after 4×10^6 s (47 days) measurements.

Discussion

We have demonstrated electrothermal control of the low-loss phase change material Sb_2Se_3 as a nonvolatile phase shifter in various reconfigurable photonic devices. Our choice of phase change materials is based on the large bandgap and the fact that Sb_2Se_3 is a single-phase compound throughout the entire solid-liquid temperature range, which, in principle, means high endurance. Considering that electrical current does not flow through the material in our approach, electromigration – a mechanism for atomic movement and failure – is also prevented. In this work, we tested the endurance of over 250 switching events, a number ultimately limited by our experimental setup; however, up to 5000 switching cycles have been demonstrated using laser pulses.³²

From simulations, we expected a phase shift of $0.09\pi/\mu\text{m}$, which was in excellent agreement with the experimental demonstrations of smaller Sb_2Se_3 cells (Fig. 1). For longer cells, the total phase modulation was slightly smaller, down to $0.08\pi/\mu\text{m}$. We attribute this discrepancy to the accumulated effect of minor thickness variations of the Sb_2Se_3 , limited by the accuracy of our deposition method (see Methods) and the non-uniformity of the heating profile. Nonetheless, we demonstrated that an ultra-compact device comprising only a $10\mu\text{m}$ -long microheater and a $6\mu\text{m}$ -long Sb_2Se_3 is enough to introduce $\pi/2$ phase shift. In turn, two $\pi/2$ nonvolatile phase shifters in a balance MZI switch, one per arm, allowed us to demonstrate another fundamental building block of programmable photonic circuits, a 2×2 optical switch (Fig. 2). We have also demonstrated the phase tunability of all-pass and add-drop micro-ring resonators to control the signals in the through and drop ports (Fig. 3), and extinction ratio modulation by engineering the coupling efficiencies to a drop port (Fig. 4). The total loss change upon switching is only $0.0005\text{ dB}/\mu\text{m}$ extracted from the ring resonator devices, which is negligible compared to the $0.03\text{ dB}/\mu\text{m}$ loss introduced by the doped-silicon microheater. The insertion loss of the phase shifter can be suppressed by further engineering the shape of the PCM cell to prevent scattering.³³ Additionally, the microheater doping profiles and geometry can also be optimized. A PIN configuration, which has demonstrated losses of $0.02\text{ dB}/\mu\text{m}$ ³⁴ can be a good alternative. Other alternatives for transparent microheaters, already demonstrated to switch PCMs, might be considered to avoid doping losses overall and extend the transparency window to shorter wavelengths, such as graphene³⁵ and indium-tin-oxide microheater;^{33,36} however, their full integration and reversible cyclability on integrated waveguides is yet to be demonstrated. We draw a direct comparison between our PCM approach and other phase shifting approaches in Table 1 considering the 10%-90% rise time, the change in effective index, Δn_{eff} , the total length and voltage to achieve a π phase shift, L_π and V_π , and the insertion loss (IL).

Table 1. Comparison of phase shifter platforms currently available in 220 nm SOI at 1550 nm. E_π is the energy required to switch and hold the state. ΔT is the temperature difference, and $t[\text{s}]$ is the time of operation.

	Δn_{eff}	$IL(\text{dB})$	$L_\pi(\mu\text{m})$	E_π	$V_\pi(V)$	Nonvolatility	Rise time ^d
Thermo-optical (doped-Si) ¹⁵	$\sim 1.8 \times 10^{-4}$ $\times \Delta T[\text{K}]$	0.23	61.6	$24.8 \times t[\text{s}] \text{ mJ}$	4.36	No	2.69 μs
Thermo-optical (metal heater) ¹⁶	$\sim 1.8 \times 10^{-4}$ $\times \Delta T[\text{K}]$	<0.4	>200	$20-25 \times t[\text{s}] \text{ mJ}$	4	No	3.7 μs
Thermo-optical with slow light ³⁷	~ 0.1	2	~ 10	$2 \times t[\text{s}] \text{ mJ}$	4.5	No	100 ns
Electro-optical (depletion) ³⁸	1.5×10^{-4}	3.6	1500	$\sim 2 \text{ pJ} \times t[\text{s}]$ ^a	10.7	No	15.5 ps
Electro-optical (injection) ³⁹	$\sim 10^{-3}$	1.5	400	$1.7 \times t[\text{s}] \text{ mJ}$	2	No	24 ns
Optoelectromechanical ¹⁷	~ 0.1	0.47	210	$22 \text{ fJ} \times t[\text{s}]$	2	No	123 ns
Liquid crystal ¹¹	0.141	0.25	49	$1 \text{ nJ} \times t[\text{s}]$	5	No	1 ms
Plasmonic nonlinear polymer ^{13c}	0.055	12	29	$60 \times t[\text{s}] \text{ fJ}$	45	No	15 ps
BTO Pockels effect ¹⁴	7×10^{-4}	1	1000	$96 \times t[\text{s}] \text{ fJ}$	3.3	No	11.7 ps
BTO Ferroelectric domain switching ²⁰	1×10^{-4}	N/A	>100	N/A	>20	Yes	100 ns
LiNbO_3 ⁴⁰	1.5×10^{-4}	2.5	5000	$170 \times t[\text{s}] \text{ fJ}$	5.1	No	3.5 ps
30 nm SbSe cladding cry/am (Here)	0.071	0.45 ^b	11	$10.24 \mu\text{J} / 185 \text{ nJ}$	3.2 / 21	Yes	0.1-1 ms / 800 ns

^a No current flows in this device, making the power dissipation extremely low. However, a constant supply of large voltage means a significant power consumption of the electronics. ^b Based on a 15 μm -long heater to switch a total of 12 μm -long Sb_2Se_3 . ^cThese values are calculated from the supplementary material of the referenced paper. ^d 10%-90% rise time. We used the single-pole approximation: $\tau = 0.35/f_{3dB}$ for results with no rise time reported.

The nonvolatility of our phase shifter guarantees zero-static power consumption – a new paradigm for photonic integrated circuits. Even if reconfigured every millisecond, our approach energy efficiency is still superior to TO phase shifters. However, if we consider only applications in which programming is done sporadically, then the energy savings are orders of magnitude different. As an example, let us consider a 512-emitter phased array containing 512 phase shifter elements whose output is reconfigured every 1s. Using our Sb_2Se_3 -based phase shifters, the average switching energy – calculated using the full crystallization pulse, which is the most energy-consuming process – would be 5.24 mJ. Since the switch is nonvolatile, the heater power consumption is just 5.24 mW since a single configuration is needed every 1s, which is three orders of magnitude lower than a constant supply of 1.9 W to modulate the lowest reported telecom wavelength beam steerer of the same size.⁴¹ The energy-saving benefit becomes even more significant with longer durations between switching events. Such nonvolatility is also interesting for configure-once applications, such as optical trimming and transient coupler for wafer-scale photonic testing.⁴²

In conclusion, we have experimentally demonstrated a new class of electrically-driven phase shifter that exploits the unique optical properties of phase-change materials to achieve zero-static power consumption in ultra-compact devices. We demonstrated several active photonic devices and applications and the potential of these devices for low-energy programmable photonic integrated circuits. Our results are promising for applications in optical trimming to correct fabrication variations and in photonic architectures with sporadic reprogramming, such as optical switching fabrics for telecommunications, phased arrays for particle trapping, photonic computing (inference with static matrices, for instance) and quantum networks, among others.

Methods

Device Fabrication

Ten 220 nm SOI wafers were fabricated with varying n -doping concentrations using the 90-nm CMOS line in Lincoln Laboratory's 200 mm wafer foundry. The doping of silicon was carried out using ion implantation of phosphorous with varying dose and implantation energy. The n^{++} region was formed with a dose of 10^{16} cm^2 and an ion energy of 80 keV. The n region of $\sim 4 \times 10^{18} \text{ cm}^{-3}$ was formed with a dose of 10^{14} cm^{-2} and an ion energy of 80 keV. The contact was fabricated with a Ti/TiN barrier following a metallization with aluminum and passivation with SiO_2 . 500 nm-wide SOI waveguides and Sb_2Se_3 cells were fabricated following two electron beam lithography fabrication steps on an Elionix ELS-F125 system. The waveguides were patterned using ZEP 520A positive photoresist followed by chlorine etching of half the silicon thickness. A lift-off process with polymethyl methacrylate (PMMA) resist was used to open the windows for the subsequent thermal evaporation of 30 nm Sb_2Se_3 . The film deposition was performed using thermal evaporation from Sb_2Se_3 bulk materials following previously established protocols.^{25,43} Bulk starting Sb_2Se_3 was synthesized using a standard melt-quench technique from high-purity (99.999%) raw elements.⁴⁴ The samples were annealed in an argon environment at 200 °C for 10 – 15 min before depositing 15 nm of Al_2O_3 by atomic layer deposition to obtain a conformal protective layer.

Experimental setup

A home-built wafer-scale automated photonic testing system was used to perform the optoelectronic measurements. A custom 18-channel SMF-28 Ultra Fiber Array with a 250 μm pitch (PLC-Connections) was used to couple light in and out of the chip using silicon-etched grating couplers. A C+L band optical vector analyzer (LUNA OVA5000) was used to scan the spectrum and carried out time-domain measurements. The high voltage electrical pulses were generated with an analog 1 GHz, 40 V pulse generator (E-H Research, HFP100) with a minimum of 0.5 ns raising and trailing edges, and the crystallization pulses with an Agilent 33250A 100Mhz pulse generator. An ACP40-AW-GSG-250 air-coplanar probe (FormFactor) was used to contact the electrical pads on the chip.

Microheater modeling

The Joule heating process and heat dissipation model were performed using a three-dimensional finite-element method simulation in COMSOL Multiphysics. We used the Semiconductors module to simulate the carrier mobility in doped silicon with the same values and shapes as our fabricated devices. We coupled this module with the Heat Transfer in Solids, where surface-to-surface radiation and thermal boundary resistance were considered. The temperature in Heat Transfer was coupled back to the semiconductor module. The mode calculations shown in Fig. 1d were carried out in Lumerical Mode, considering the Sb_2Se_3 refractive index shown in Fig. 1b and the built-in refractive indices for Si, Al_2O_3 , and SiO_2 .

Acknowledgments

This material is based upon work supported by the DARPA Young Faculty Award Program under Grant Number D18AP00070, the Assistant Secretary of Defense for Research and Engineering under Air Force Contract No. FA8702-15-D-0001, and Draper Laboratory. The authors acknowledge fabrication facility support by the MIT Microsystems Technology Laboratories, the Materials Research Laboratory, and the Lincoln Laboratory Microelectronic Laboratory.

References

1. Bogaerts, W. *et al.* Programmable photonic circuits. *Nature* **586**, 207–216 (2020).
2. Carolan, J. *et al.* Universal linear optics. *Science (80-.).* **349**, 711–716 (2015).
3. Cheng, Q., Rumley, S., Bahadori, M. & Bergman, K. Photonic switching in high performance datacenters [Invited]. *Opt. Express* **26**, 16022 (2018).
4. Cheng, Q., Bahadori, M., Glick, M., Rumley, S. & Bergman, K. Recent advances in optical technologies for data centers: a review. *Optica* **5**, 1354 (2018).
5. Sun, J., Timurdogan, E., Yaacobi, A., Hosseini, E. S. & Watts, M. R. Large-scale nanophotonic phased array. *Nature* **493**, 195 (2013).
6. Kita, D. M. *et al.* High-performance and scalable on-chip digital Fourier transform spectroscopy. *Nat. Commun.* **9**, 1–7 (2018).
7. Shen, Y. *et al.* Deep learning with coherent nanophotonic circuits. *Nat. Photonics* **11**, 441–446 (2017).
8. Arrazola, J. M. *et al.* Quantum circuits with many photons on a programmable nanophotonic chip. *Nature* **591**, 54–60 (2021).
9. Reed, G. T., Mashanovich, G., Gardes, F. Y. & Thomson, D. J. Silicon optical modulators. *Nat. Photonics* **4**, 518–526 (2010).
10. Witzens, J. High-Speed Silicon Photonics Modulators. *Proc. IEEE* **106**, 2158–2182 (2018).
11. Pfeifle, J., Alloatti, L., Freude, W., Leuthold, J. & Koos, C. Silicon-organic hybrid phase shifter based on a slot waveguide with a liquid-crystal cladding. *Opt. Express* **20**, 15359 (2012).
12. De Cort, W., Beeckman, J., Claes, T., Neyts, K. & Baets, R. Wide tuning of silicon-on-insulator ring resonators with a liquid crystal cladding. *Opt. Lett.* **36**, 3876–3878 (2011).
13. Melikyan, A. *et al.* High-speed plasmonic phase modulators. *Nat. Photonics* **8**, 229–233 (2014).
14. Abel, S. *et al.* Large Pockels effect in micro- and nanostructured barium titanate integrated on silicon. *Nat. Mater.* **18**, 42–47 (2019).
15. Harris, N. C. *et al.* Efficient, compact and low loss thermo-optic phase shifter in silicon. *Opt. Express* **22**, 10487 (2014).
16. Jacques, M. *et al.* Optimization of thermo-optic phase-shifter design and mitigation of thermal crosstalk on the SOI platform. *Opt. Express* **27**, 10456 (2019).
17. Grottko, T., Hartmann, W., Schuck, C. & Pernice, W. H. P. Optoelectromechanical phase shifter with low insertion loss and a 13π tuning range. *Opt. Express* **29**, 5525 (2021).
18. Grajower, M., Mazurski, N., Shappir, J. & Levy, U. Non-Volatile Silicon Photonics Using Nanoscale Flash

- Memory Technology. *Laser Photonics Rev.* **12**, 1–8 (2018).
19. Errando-Herranz, C. *et al.* MEMS for Photonic Integrated Circuits. *IEEE J. Sel. Top. Quantum Electron.* **26**, (2020).
20. Abel, S. *et al.* Multi-level optical weights in integrated circuits. *2017 IEEE Int. Conf. Rebooting Comput. ICRC - Proc.* 1–3 (2017). doi:10.1109/ICRC.2017.8123672
21. Wuttig, M., Bhaskaran, H. & Taubner, T. Phase-change materials for non-volatile photonic applications. *Nat. Photonics* **11**, 465–476 (2017).
22. Abdollahramezani, S. *et al.* Tunable nanophotonics enabled by chalcogenide phase-change materials. *Nanophotonics* **9**, 1189–1241 (2020).
23. Wang, J., Wang, L. & Liu, J. Overview of Phase-Change Materials Based Photonic Devices. *IEEE Access* **8**, 121211–121245 (2020).
24. Rios, C. *et al.* Integrated all-photonic non-volatile multi-level memory. *Nat. Photonics* **9**, 725–732 (2015).
25. Zhang, Y. *et al.* Broadband transparent optical phase change materials for high-performance nonvolatile photonics. *Nat. Commun.* **10**, 2–3 (2019).
26. Dong, W. *et al.* Wide Bandgap Phase Change Material Tuned Visible Photonics. *Adv. Funct. Mater.* **29**, 1806181 (2019).
27. Delaney, M., Zeimpekis, I., Lawson, D., Hewak, D. W. & Muskens, O. L. A New Family of Ultralow Loss Reversible Phase-Change Materials for Photonic Integrated Circuits: Sb₂S₃ and Sb₂Se₃. *Adv. Funct. Mater.* **30**, 2002447 (2020).
28. Li, Y. *et al.* Coupled-ring-resonator-based silicon modulator for enhanced performance. *Opt. Express* **16**, 13342 (2008).
29. Zhang, Y. *et al.* Myths and Truths about Optical Phase Change Materials: A Perspective. To appear in *Appl. Phys. Lett.* (2021).
30. Rios, C. *et al.* Controlled switching of phase-change materials by evanescent-field coupling in integrated photonics. *Opt. Mater. Express* **8**, 2455–2470 (2018).
31. Ríos, C. *et al.* In-memory computing on a photonic platform. *Sci. Adv.* **5**, eaau5759 (2019).
32. Delaney, M. *et al.* Non-volatile programmable silicon photonics using an ultralow loss Sb₂Se₃ phase change material. *arXiv:2101.03623* (2021).
33. Taghinejad, H. *et al.* ITO-Based Microheaters for Reversible Multi-Stage Switching of Phase-Change Materials: Towards Miniaturized Beyond-Binary Reconfigurable Integrated Photonics. *ArXiV Prepr.* arXiv:2003.04097 (2020).
34. Zheng, J. *et al.* Nonvolatile Electrically Reconfigurable Integrated Photonic Switch Enabled by a Silicon PIN Diode Heater. *Adv. Mater.* 2001218 (2020). doi:10.1002/adma.202001218
35. Ríos, C. *et al.* Multi-Level Electro-Thermal Switching of Optical Phase-Change Materials Using Graphene. *Adv. Photonics Res.* **2**, 2000034 (2020).
36. Kato, K., Kuwahara, M., Kawashima, H., Tsuruoka, T. & Tsuda, H. Current-driven phase-change optical gate switch using indium-tin-oxide heater. *Appl. Phys. Express* **10**, (2017).
37. Vlasov, Y. A., O’Boyle, M., Hamann, H. F. & McNab, S. J. Active control of slow light on a chip with photonic crystal waveguides. *Nature* **438**, 65–69 (2005).
38. Zhang, F. *et al.* Toward single lane 200G optical interconnects with silicon photonic modulator. *J. Light. Technol.* **38**, 67–74 (2019).
39. Kang, G. *et al.* Silicon-Based Optical Phased Array Using Electro-Optic Phase Shifters. *IEEE Photonics Technol. Lett.* **31**, 1685–1688 (2019).
40. He, M. *et al.* High-performance hybrid silicon and lithium niobate Mach-Zehnder modulators for 100 Gbit s⁻¹ and beyond. *Nat. Photonics* **13**, 359–364 (2019).
41. Miller, S. A. *et al.* Large-scale optical phased array using a low-power multi-pass silicon photonic platform. *Optica* **7**, 3 (2020).
42. Zhang, Y. *et al.* Transient tap couplers for wafer-level photonic testing based on optical phase change materials. *Submitted* (2020).
43. Hu, J. *et al.* Fabrication and testing of planar chalcogenide waveguide integrated microfluidic sensor. *Opt. Express* **15**, 2307 (2007).
44. Petit, L. *et al.* Compositional dependence of the nonlinear refractive index of new germanium-based chalcogenide glasses. *J. Solid State Chem.* **182**, 2756–2761 (2009).